

INVESTIGATION OF CROSS-FLOW EFFECTS REGARDING LAMINAR FLOW CONTROL WITHIN CONCEPTUAL AIRCRAFT DESIGN

Florian Schuelcke

Institute of Aerospace Systems,
RWTH Aachen University
Wuellnerstrasse 7
52062 Aachen, Germany
schuelcke@ilr.rwth-aachen.de

Eike Stumpf

Institute of Aerospace Systems,
RWTH Aachen University
Wuellnerstrasse 7
52062 Aachen, Germany
stumpf@ilr.rwth-aachen.de

Abstract. This paper presents the results of investigating the accuracy of 2D methods for estimating laminar flow regions on 3D wing objects. Since laminar flow highly depends on cross-flow effects, several methods, relating 3D and 2D flow conditions, are analyzed with regard to capturing these cross-flow influences. The 3D pressure distributions depending on the utilized transformation method analyzed and compared to RANS solutions. With the most precise transformation method, the laminar flow area on a conventional wing of a short range aircraft is determined and compared to the laminar area obtained with the RANS pressure distributions as input. Further, HLFC component sizing is analyzed to obtain the net benefit in fuel reduction of simplified method compared to RANS method for a conventional short range aircraft. In this particular case, the potential in fuel reduction calculated with simplified methods is only half of that calculated with RANS.

Keywords. cross-flow, transformation methods, laminar flow, hybrid laminar flow control, conceptual aircraft design.

1 Introduction

Aiming at sustainable air transportation, challenging goals have been defined in different strategic documents. The most prominent goal being a reduction of CO₂ emissions by 75 % until the year 2050 (with reference to 2000) is published in the ACARE-document "Flightpath 2050". This poses strong requirements to manufacturers and operators to substantially increase aircraft fuel efficiency [9]. Besides improvements in aircraft operation and air traffic management the goal can be reached on aircraft level by working on the classical three technology levers, i.e. structural mass, propulsion system and aerodynamics.

Regarding the field of aerodynamics, laminarization of aircraft surfaces is the most promising technology [20]. An increased portion of laminar flow on aircraft surfaces leads to a reduced friction drag. The drag reduction potential is highest for the main wing of the aircraft. On swept wings of transport aircraft, transition from laminar to turbulent flow is mainly governed by three instability mechanisms: Tollmien-Schlichting instability (TSI), cross-flow instability (CFI) and attachment line transition (ALT). They can occur alone or in combination, which is strongly dependent on Reynolds number and wing sweep angle. Beyond certain combinations of Reynolds and Mach number sufficient laminar flow can only be reached by a combination of specific airfoil shape and an active control system, known as hybrid laminar flow control.

1.1 Problem

Due to the high Mach and Reynolds numbers of today's transport aircraft and thus, highly swept wings, CFI have to be taken into account. CFI develop closely behind the wing leading edge. To suppress CFI a suction system in that region is a possible option. The size of this suction system, and therefore its mass and power offtakes, depends on the required strength of suction. This results in drawbacks regarding additional system mass and power offtakes on the engines. Thus, it is essential to evaluate hybrid laminar flow control on overall aircraft level.

To be able to capture three-dimensional effects, such as cross-flow and the related instabilities, highly sophisticated methods are needed. While streamwise transition prediction with respect to TSI is often found to be implemented in airfoil or low-sweep wing design tools, a simultaneous reliable coverage of CFI for highly swept and tapered wing applications is rarely included within preliminary aircraft design, since the required accurate and time-consuming computations are not an option for the application within conceptual or preliminary aircraft design. This raises the questions a) how the existing approaches and specifically the implemented transformations differ from each other, b) if and in which way simple estimations and simplifications could be used and c) where the limits are, i.e. how far they are from reality.

1.2 Approach

In order to answer these questions and to derive an approach for conceptual aircraft design, in this paper first of all different transformation methods will be analyzed and validated for several applications. As simplification for infinite swept wings, often the so-called "simple sweep theory" (SST) is used, which is based on early swept wing investigations by Busemann and provides transformation rules between 3D and 2D geometry and flow conditions [4]. Since these simple 2D transformations neglect significant flow phenomena occurring on tapered wing geometries, for the more realistic case of a tapered wing also several approaches have been developed. Based on SST, some models use the shock position as an additional input, which is unfortunately itself influenced by 3D effects of the flow field. [3]

Another proposed method uses a conical 2.5D approach. It combines equations of sweep taper theory, i.e. an enhancement of simple sweep theory for tapered wing geometries, with conical flow assumptions. The latter are used for relating 2D and 3D pressure distributions, and are also the basis for formulation and solution of the compressible conical boundary layer equations. [30]

In the present investigation for all these transformation methods 2D pressure distributions will be calculated with the flow solver MSES [8]. For this purpose, an automated in-house method is used to transform freestream conditions as well as wing geometry, generate 2D flow solutions at discrete wing sections with MSES and translate the resulting 2D pressure distribution into a 3D pressure distribution. This will be done for different wings with increasing complexity: starting with an unswept rectangular wing, then including wing sweep and taper ratio, and finally investigating a standard airliner kinked wing. The results will be compared and validated with a 3D CFD solution using RANS. (see sec. 3)

In a second stage the different pressure distributions will be used as input for transition prediction. The results will be compared among each other and to 3D CFD solutions for wing sections of a kinked 3D wing. Cross-flow does have an impact on the pressure distribution of the wing and with this on the CFI as transition mechanism and therefore on the transition line. The contribution of the laminar flow area of the wing to the friction drag will be analyzed on overall aircraft level with the in-house conceptual aircraft design and optimization environment MICADO [18]. For a short range reference aircraft [5] the overall benefit will be evaluated in terms of block fuel, including the benefit of drag reduction as well as possible drawbacks of mass growth due to the additional system mass and snowball effects on the one hand and the influence on the engine performance due to power offtakes on the other hand. (cf. sec. 4)

As a further approach, it will be analyzed if suppression of CFI by increasing suction strength, resulting in increasing generator masses and power offtakes, will be more beneficial regarding fuel consumption than smaller generators and less aerodynamic efficiency.

2 Fundamentals

This section provides the fundamentals regarding cross-flow, its impact on pressure distribution of the wing as well as the influence of pressure distributions on laminar flow. Furthermore, the transformation methods, utilized in this paper, are presented.

2.1 Development of cross-flow

Cross-flow is mainly induced by two effects. Applying a sweep angle to a wing is done often for high freestream Mach numbers to reduce drag rise, since for pressure induced drag only the velocity component perpendicular to the line of constant pressure is important. Hence, this component is a reduced freestream velocity by the cosine of the effective sweep angle at this location. In case of wing sweep not only a velocity component perpendicular to the pressure line occurs but also a component parallel to the line of constant pressure in the direction of wing span exists (cf. Figure 1).

In addition, cross-flow is triggered at the wing tip due to pressure compensation. The lift force of a wing is produced by a difference in pressure between the upper and lower surface. This difference in pressure compensates at the wing tip. Thereby a vortex is induced and dependent on the spanwise position streamlines on the lower wing surface are deflected towards the wing tip whereas the streamlines on the upper wing surface are deflected towards the wing root, i.e. for the case of a backward swept wing the tip induced cross-flow to some extent counteracts the sweep-induced cross-flow on the upper wing surface and adds to it on the lower wing surface, respectively.

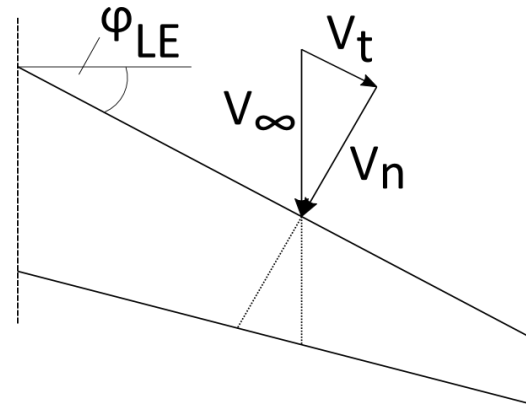


Figure 1: Velocity components due to wing sweep.

2.2 Pressure distribution and instabilities

With regard to laminar flow, the transition is mainly governed by three instability mechanisms:

- Tollmien-Schlichting instabilities (TSI)
- cross-flow instabilities (CFI)
- attachment line transition (ALT)

Figure 2 indicates, in which regions these forms of instability occur. TSI are waves which travel in streamwise direction and strongly amplify behind the maximum thickness of the wing. The positive pressure gradient in this region produces an inflection point in the velocity profile which is destabilizing for TS-waves. [11, 22] CFI-waves primarily occur in regions with strong negative pressure gradient, e.g. behind the wing leading edge as presented in Figure 2 [21]. Thus, pressure gradients damping TSI-waves are amplifying CFI-waves. For leading edge sweep angles higher than about $\varphi_{LE} \geq 30^\circ$ CFI are dominant to TSI.

To suppress CFI and TSI, several techniques are available. On the one hand side, the flow around the airfoil can be influenced in a passive way by a favorable airfoil design, which is called “natural laminar flow” (NLF). The negative pressure gradient due to high velocities behind the leading edge can be influenced by changing the thickness and camber of the airfoil. Laminar wings are thinner and the leading edge region is more pointed. The maximum thickness occurs at 40-50 % of local chord, whereas the maximum thickness of turbulent wings is often located at about 25 % local chord. [23] However, for highly swept wings this technique is insufficient to suppress CFI, in this case CFI has to be actively suppressed. By suction of the boundary layer behind the leading edge, the flow velocity is decreased and the flow is stabilized. This technique is called “laminar flow control” (LFC). The combination of NLF and LFC technique is called “hybrid laminar flow control” (HLFC).

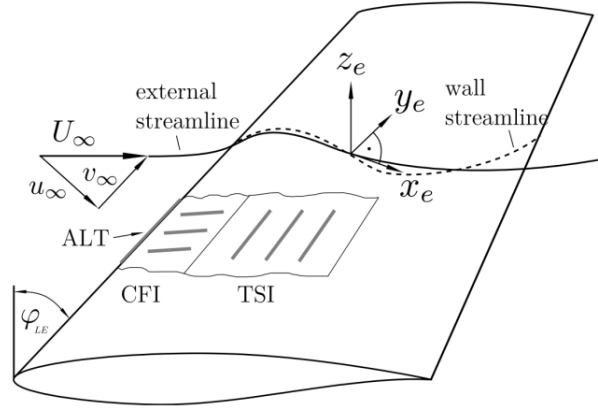


Figure 2: Instability mechanisms for three-dimensional flow around a swept wing, adopted from [10].

The attachment line transition is not further investigated within this paper. For further details, it is referred to [17, 28].

2.3 Transformation methods relating 2D and 3D flow conditions and geometry

As mentioned in the introductory part of this paper, for conceptual aircraft design often a full 3D flow solution is too expensive with respect to required computation time and modeling effort. To be able to simplify aerodynamic calculations of conventional wings with 2D flow solver, the flow conditions has to be transformed. On the other hand, such simple 2D transformations neglect significant flow phenomena occurring on tapered wing geometries. In this section some transformation methods are presented, which are used in the following section to calculate 2D solutions of the flow on a 3D wing.

For an infinite swept wing the so-called “simple sweep theory” (SST) [4] provides a transformation rule for flow and geometry conditions. The equivalent 2D Mach number is defined as:

$$\text{Ma}_{2\text{D}} = \text{Ma}_{3\text{D}} \cdot \cos(\varphi_{\text{eff}}) \quad (\text{Eq.1})$$

with φ_{eff} as an effective sweep angle of a 3D wing object used for transformation. As the overall lift on the wing keeps constant, as well as the surface and the density, Eq. 2

$$\frac{\rho}{2} \cdot v_n^2 \cdot S_{\text{ref}} \cdot C_{L,2\text{D}} = \frac{\rho}{2} \cdot v_\infty^2 \cdot S_{\text{ref}} \cdot C_{L,3\text{D}} \quad (\text{Eq.2})$$

can be converted with $v_n = v_\infty \cdot \cos(\varphi_{\text{eff}})$ into

$$C_{L,2\text{D}} = \frac{C_{L,3\text{D}}}{\cos^2(\varphi_{\text{eff}})}. \quad (\text{Eq.3})$$

Accordingly, the angle of attack can be written as

$$\alpha_{2\text{D}} = \frac{\alpha_{3\text{D}}}{\cos(\varphi_{\text{eff}})}. \quad (\text{Eq.4})$$

With reducing the flow in one dimension, the influence of the cross-flow component has to be integrated in another way. For this reason, Eq.1 has been extended to

$$\text{Ma}_{2D} = \text{Ma}_{3D} \cdot \cos^x(\varphi_{\text{eff}}), \quad (\text{Eq.5})$$

where the variable 'x' in the exponent is set to 1 for infinite swept wings and '0' for no transformation. Several values for 'x' are proposed by [1, 29, 31], but there is no definition in general. Equally, Eq.4 is enhanced to

$$\alpha_{2D} = \frac{\alpha_{3D}}{\cos^x(\varphi_{\text{eff}})}. \quad (\text{Eq.6})$$

This raises the question, how to define the effective sweep angle φ_{eff} . For infinite swept wings, the choice of the transformation sweep angle is unique. But for more realistic wings with varying sweep angle in chordwise direction, Boppe [3], Küchemann [12] and van Der Velden [32] have shown, that for transonic flow over swept tapered wings, the local sweep angle of shock position (or recompression area) serves well as transformation angle. The extension of SST for application to finite tapered wings is commonly called sweep taper theory (STT).

Next to flow conditions also the geometry has to be transformed to perform 2D calculations. In the context of SST, the airfoil for the 2D solution has to be considered in a direction normal to the wing leading edge. Therefore, the chord length and thereby the thickness ratio of the wing will change in accordance with Eq.7:

$$\left(\frac{z}{c}\right)_{2D} = \frac{1}{\cos(\varphi)} \cdot \left(\frac{z}{c}\right)_{3D} \quad (\text{Eq.7})$$

For tapered wings, local sweep angle is a function of relative chord with

$$\tan(\varphi) = \tan(\varphi_{\text{LE}}) \cdot \left(1 - \frac{x}{c}\right) + \tan(\varphi_{\text{TE}}) \cdot \frac{x}{c}. \quad (\text{Eq.8})$$

With Eq.7 and Eq.8 the conical transformation is defined as

$$\left(\frac{z}{c}\right)_{2D} = \sqrt{1 + \left[\tan(\varphi_{\text{LE}}) \cdot \left(1 - \frac{x}{c}\right) + \tan(\varphi_{\text{TE}}) \cdot \frac{x}{c} \right]^2} \cdot \left(\frac{z}{c}\right)_{3D}. \quad (\text{Eq.9})$$

To be able to use pressure distributions from a 2D flow solver within 3D wing design objects, an equivalence law, relating 2D and 3D pressure distributions, formulated by Lock is used [16]. Derived from the relation between 2D and 3D pressure distributions for infinite swept wings,

$$c_{p,3D} = c_{p,2D} \cdot \cos^{2x}(\varphi_{\text{eff}}), \quad (\text{Eq.10})$$

and the assumption of conical flow, i.e. the isobars are aligned with the constant percent-chord sweep angles, Lock derived Eq.11 for transformation of 2D pressure distributions:

$$c_{p,3D} = \frac{f-1}{\frac{\gamma}{2} \cdot \text{Ma}_{3D}^2} + f \cdot c_{p,2D} \cdot \cos^{2x}(\varphi_{\text{eff}}), \quad (\text{Eq.11})$$

where f is denoted as

$$f = \left[\frac{1 + \frac{\gamma-1}{2} \cdot (\text{Ma}_{3D} \cdot \cos(\varphi_{x/c}))^2}{1 + \frac{\gamma-1}{2} \cdot (\text{Ma}_{3D} \cdot \cos^x(\varphi_{\text{eff}}))^2} \right]^{\frac{\gamma}{\gamma-1}}, \quad (\text{Eq.12})$$

with γ as the ratio of specific heat of air and $\varphi_{x/c}$ as the local sweep angle at the corresponding relative chordwise position.

In the following section, for the transformation of freestream conditions, Eq.5 and Eq.6, are used with varying values for the exponent 'x', as well as Eq.7 and Eq.9 for the transformation of the airfoil geometry.

3 Pressure distributions of reference wings

In this section, the methods relating 3D and 2D properties of geometry, freestream and pressure distribution are analyzed. In a first step the reference wings are defined (cf. sec. 3.1) with increasing complexity. Next, the flow around the wings is calculated with two different flow solvers. On the one hand, MSES is used, which is a 2D Euler-code with boundary layer coupling capable to estimate friction drag. Furthermore, MSES offers the possibility to specify laminar flow areas in order to consider partly laminar flow around the airfoil. MSES was developed by Mark Drela from MIT. For further details the reader is referred to the user guide [8] and related publications [6, 7]. In this paper MSES is used to calculate the pressure distribution for given freestream conditions at several spanwise sections of the different wings. To get a 3D solution, Lock's law is utilized, relating 2D and 3D pressure distributions (cf. Eq.11) [16]. The influence of geometric modifications on the rectangular wing to the pressure distribution by adding a sweep angle or a taper ratio as well as the combination of both is shown in sec. 3.2.

On the other hand, 3D CFD calculations of the wings are performed. For this purpose, the DLR-TAU code is utilized, employing the RANS equations, using a backward Euler-scheme and the Spalart Allmaras (one-equation) turbulence model. For comparison of the resulting pressure distributions, surface cuts are extracted from the 3D CFD solutions. (cf. sec. 3.3)

3.1 Reference wings and airfoil

For the reference wings, simple geometries are selected. The three-dimensional wings emerge from the definition of the airfoil geometries and a linear lofting between them. All wings use as basic airfoil the extracted airfoil geometry of the wing of the Common Research Model [33] at 37 % of halfspan. The first wing is a rectangular wing (1) with a halfspan of $s=15\text{ m}$ and a mean aerodynamic chord of $MAC=6\text{ m}$. Applying a leading edge sweep angle of $\varphi_{LE}=16^\circ$ to the rectangular wing delivers the swept reference wing (2) with the same half span and MAC. (cf. Figure 3)

The third reference wing is a tapered wing (3) with a taper ratio of $\lambda=0.25$ and an inner chord of $c_{root}=6\text{ m}$ and a tip chord of $c_{tip}=1.5\text{ m}$, correspondingly. The center line is perpendicular to the root and tip chord which involves a leading edge sweep of $\varphi_{LE}=8.53^\circ$ and a trailing edge sweep angle of $\varphi_{TE}=-8.53^\circ$, respectively and a mean aerodynamic chord of $MAC=4.2\text{ m}$. The fourth reference wing is created by applying a sweep of $\varphi_{LE}=16^\circ$ (4) to reference wing No.3. Keeping all other parameters constant, this results in a trailing edge sweep of $\varphi_{TE}=-0.76^\circ$. (cf. Figure 4 (left figure))

Assembling two tapered wings ends up in a so-called kinked wing (5) as found on conventional transport aircraft. The wing with the highest complexity complies with the previous wings in a root chord of $c_{root}=6\text{ m}$ and a tip chord of $c_{tip}=1.5\text{ m}$. The mean aerodynamic chord is calculated to $MAC=3.73\text{ m}$ and the kink is located at 29 % of half span which is at $y_{kink}=4.37\text{ m}$. In order to be

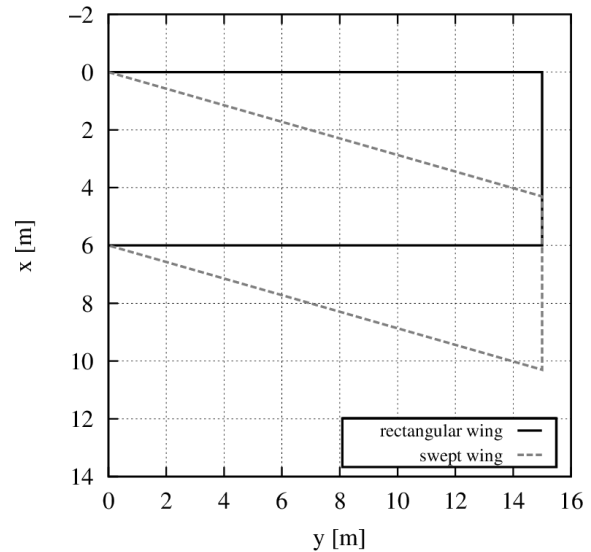


Figure 3: Rectangular and swept reference wing.

able to fit the wing to the reference aircraft for final investigations of laminar flow area, the sweep back of the wing is increased from $\varphi_{LE} = 16^\circ$ to $\varphi_{LE} = 27^\circ$. (cf. Figure 4 (right figure))

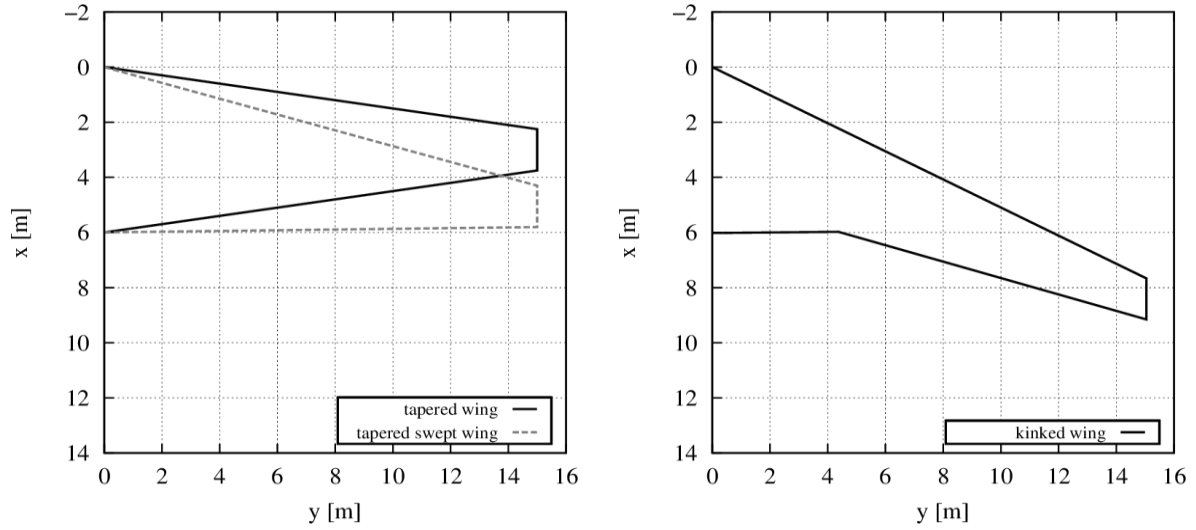


Figure 4: Tapered, tapered-swept and kinked reference wing.

For flow analysis, three sections at relative half span positions of $\eta_1 = 0.00006$ near the root chord, $\eta_2 = 0.4973$ in the middle of each wing and $\eta_3 = 0.9913$ in the outer most region of the wing are examined.

The Mach number of freestream is set to $Ma = 0.78$ and the temperature to $T = 218.81\text{K}$ in accordance with the temperature at 35 000 ft.

3.2 Influence of transformation methods on pressure distributions

In order to study different transformation methods parameter studies with respect to freestream conditions, geometrical and methodological variables were performed. These parameters were varied as listed in Table 1. For each parameter combination a pressure distribution was calculated with the 2D flow solver MSES.

Table 1: Parameter variations for MSES calculations

Parameter	Range
Spanwise position of section [% of halfspan]	0.00006, 0.4973, 0.9913
Angle of attack	$0^\circ, 1^\circ, 2^\circ$
Geometrical transformation	none, SST, conical
Exponent 'x' for freestream conditions	from 0.0 to 1.0 with a step size of 0.1
Location of φ_{eff} [% of local chord]	from 0.0 to 1.0 with a step size of 0.1

The parameter combination amount to 3267 data points for each wing. For reasons of clarity, not each data point is presented in the figures below. The figures only illustrate the cases affected by the special wing geometry.

Figure 5 presents the reference pressure distributions for the rectangular wing. For all cases examined, the only parameter influencing the pressure distribution is the angle of attack. Since all transformation formulas for geometrical transformation as well as for transformation of freestream conditions and the relation between 2D and 3D pressure distributions depend on the sweep angle of the wing, which is equal to zero in this case, no influence of transformation methods as SST, STT (cf. sec. 2.3) on pressure distributions can be seen. Also the chord at each section is the same and thus, the pressure distributions for each section coincide. Due to high Mach number and no leading edge sweep, a shock occurs for recompression. With α increased, the shock moves downstream to a relative chord of about 65 %.

The small oscillations in the pressure distributions, especially in the case of $\alpha=0^\circ$, result from slight oscillations of the point distribution of the investigated airfoil. Since it has no further influence on the results of this paper, they will be ignored in all further studies. For all following test cases, the influences of the several transformations are analyzed only for an angle of attack of $\alpha=0^\circ$. This is done again for reasons of clarity as the findings are identical for the other angles of attack.

The influence of leading edge sweep on the pressure distribution is depicted in Figure 6. For a value of '0' for the exponent 'x' ("flow trans" off) and SST as well as Lock-method switched off, the case correlates to the cases of rectangular wing (cf. blue line and light gray squares in Figure 6). If the SST transformation is activated, the related 2D airfoil becomes thicker. This results in an increasing velocity around the airfoil, shifting the pressure distribution upwards and the shock position downstream compared to the reference (cf. black crosses in Figure 6). Since in this case the leading edge and trailing edge sweep angle are the same, Eq.9 migrates to Eq.7. Thus, there is no difference between SST and conical geometrical transformation. It can be observed that only the transformation of the flow conditions in terms of the exponent has a remarkable influence (cf. small gray dots in Figure 6). With increasing value of the exponent, the cosine in Eq.5 and 6 decreases, since the value is below 1. This results in a lower freestream Mach number for the 2D calculation but a higher angle of attack. As only an angle of attack of zero degree is investigated in this case, the transformation of the angle of

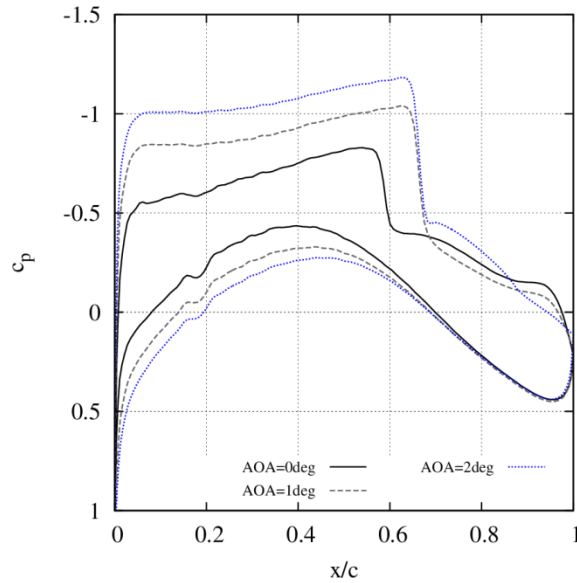


Figure 5: Comparison of pressure distributions for rectangular wing.

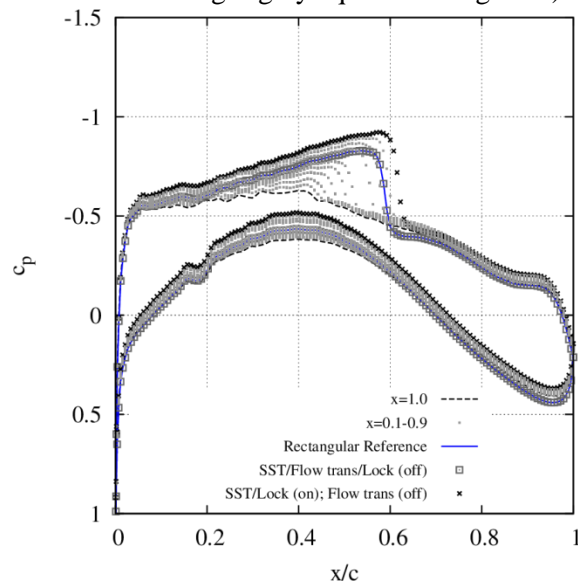


Figure 6: Comparison of pressure distributions for swept wing.

attack has no impact on the pressure distribution. Thereby, the 2D Mach number can be reduced to such a level, that the shock weakens until it becomes an isentropic recompression area. This transformation allows for considering cross-flow due to wing sweep, which affect the streamwise velocity in the region of the leading edge and with that for the whole flow around the airfoil. To consider cross-flow due to tip vortices, which influence the streamwise velocity often behind the leading edge, is not possible with this method.

For the tapered wing not only a variation of Reynolds length but also a variation of sweep angle in streamwise direction becomes relevant. Tapering automatically meant reducing the trailing edge sweep angle and thus, thinning the equivalent 2D airfoil compared to a not tapered wing with the same leading edge sweep angle.

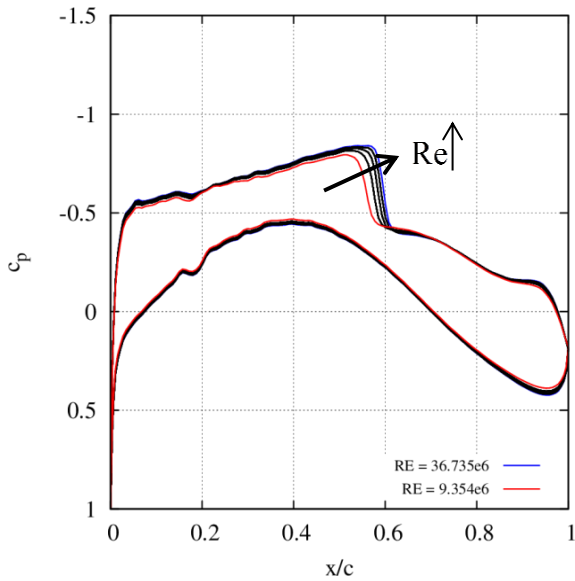


Figure 7: Comparison of pressure distributions for tapered wing – Reynolds length.

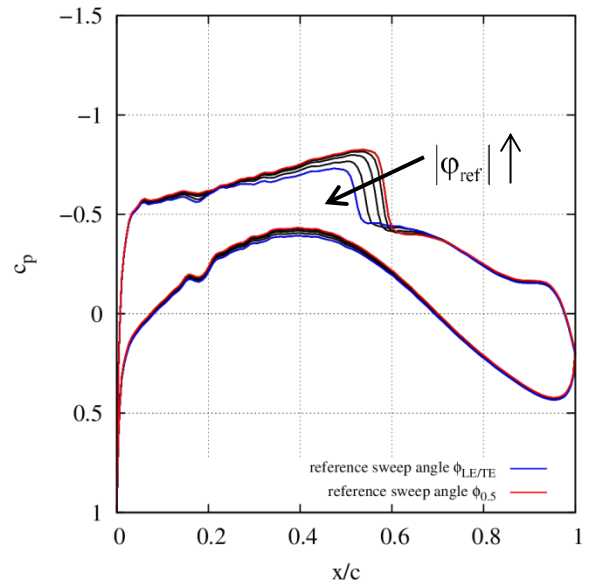


Figure 8: Comparison of pressure distribution for tapered wing – variation of transformation sweep.

Figure 7 illustrates the variation of pressure distribution on a tapered wing for increasing Reynolds number. With increasing Reynolds length, the shock moves slightly downstream, whereas the opposite is shown in Figure 8. If the streamwise transformation location increases, which is equivalent to increasing effective sweep angle for transformation, the shock moves upstream and is weakened. This is due to the fact that 2D Mach number is decreasing with higher transformation angles.

As for tapered wings the trailing edge and leading edge sweep angle are not the same, the conical transformation according to Eq.9 has an influence on the pressure distribution as mentioned above. By enlarging the airfoil with applying conical transformation rules less than with SST, the gradient of streamwise velocity is not as high in the region of maximum thickness. This implicates also a slightly weaker shock as it can be seen in Figure 9. Figure 10 repeats the result of Figure 9. While having the same leading edge sweep, the pressure curve for the tapered swept wing (cf. blue line in Figure 10) is shifted to higher pressure values compared to the red line representing the swept wing without taper ratio due to a lower trailing edge sweep and hence, a thinner equivalent 2D airfoil. The influence of conical transformation gets stronger with increasing difference of leading and trailing edge sweep.

The influences of transformation methods on the kinked wing are comparable to those of the swept-tapered one. For this reason, there will be no discussion of the kinked wing at this point but in the next section, which compares the pressure distributions calculated with TAU.

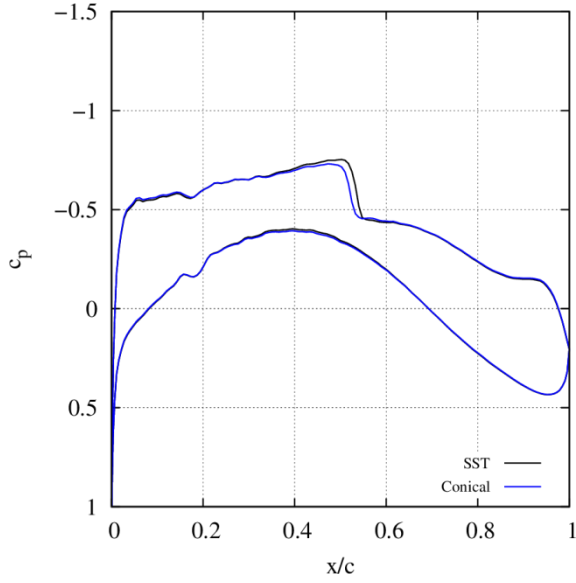


Figure 9: Comparison of pressure distributions for tapered wing – SST vs. conical.

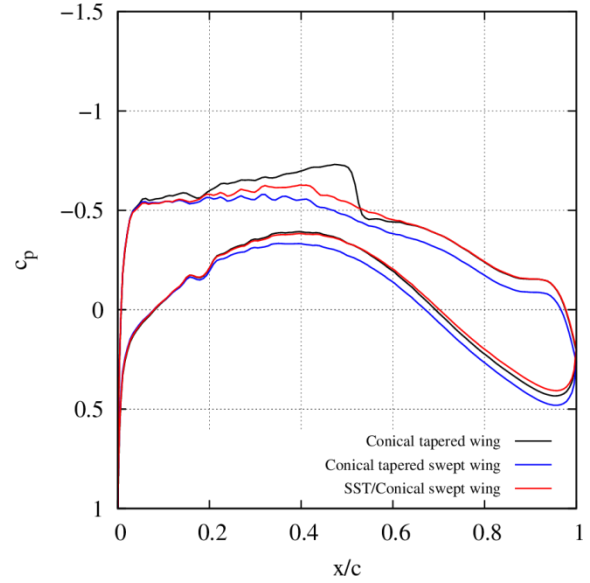


Figure 10: Comparison of pressure distribution for swept, tapered and tapered-swept wing.

3.3 Comparison of MSES to TAU

For 3D solutions of the flow around the reference wings, the flow solver TAU is used for solving the RANS equations, using a backward Euler-scheme and the Spalart Allmaras (one-equation) turbulence model. The flow conditions used for calculations are listed in Table 2.

Table 2: Global values for flow calculation

Wing#	(1)	(2)	(3)	(4)	(5)
Mach number [-]			0.78		
Temperature [K]			218,81K		
Reference length [m]	6	6	4.2	4.2	3.73
Reynolds number [-]	36.753e6	36.753e6	25.727e6	25.727e6	22.854e6

For each wing, the MSES pressure distribution closest to the TAU pressure distribution is presented for each section on the wing. In each figure the TAU solutions are marked with blue triangles for the root section at $\eta_1 = 0.00006$, red circles at $\eta_2 = 0.4973$ and light gray circles at $\eta_3 = 0.9913$.

Starting with the rectangular wing, Figure 11 shows a deviation of MSES and TAU pressure distributions to a considerable degree. First of all, it can be seen, that the TAU pressure distributions are different for each section, which deviates from the MSES solution (cf. sec. 3.2). Here the first drawback of 2D solutions becomes apparent, which are not able to consider cross-flow initiated by a tip vortex. The presence of such a tip vortex in this case is shown in Figure 12. In this figure the velocity distribution in x-direction (cf. Figure 12(a)) and y-direction (cf. Figure 12(b)) over the wing at a station of $x/c = 0.5$ are presented. Regarding the pressure distributions, the velocity in x-direction is important. On the left hand side of Figure 12, an increasing velocity on the wing upper side in direction of the flow, starting at the wing tip in spanwise direction to the wing root, can be

constituted. The velocity in x-direction is decreased at the tip segment by a flow component in spanwise direction from tip to root, which can be seen on the right hand side of Figure 12, where remarkably higher values of velocity in negative y-direction can be noticed. This indicates a tip vortex, which starts at about 25% local chord. The existence of the vortex can be underlined with the pressure distribution of the slice near the tip region in Figure 11. The gray dotted curve indicates the same amount of pressure between $x/c = 0.2$ and $x/c = 0.6$. Behind $x/c = 0.6$ flow separation occurs. With decreasing spanwise position, it can be noticed that the pressure distributions coincide in the region of leading edge up to 20% local chord, since no induced y-component of velocity is available, as it can be assumed for rectangular wings. Starting from here up to x/c of about 60% the curves move slightly away from each other at the wing upper side. This is due to the induced y-component of the velocity, caused by the tip vortex, which decreases the streamwise velocity from about 30% of halfspan to tip. These effects are fully neglected by the MSES solution.

Compared to TAU, the overall pressure gradients calculated with MSES are much higher, which requires a high recompression archived by a strong shock at $x/c = 0.59$. Here the pressure distribution corresponds to each other. The trend of the pressure distributions points out a high negative pressure gradient, which tends the flow to change from laminar to turbulent flow due to CFI. This trend is also covered by the resulting pressure distribution of MSES calculation.

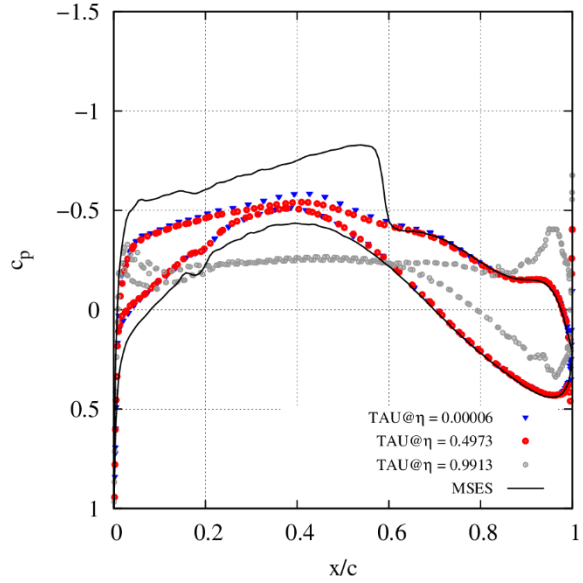
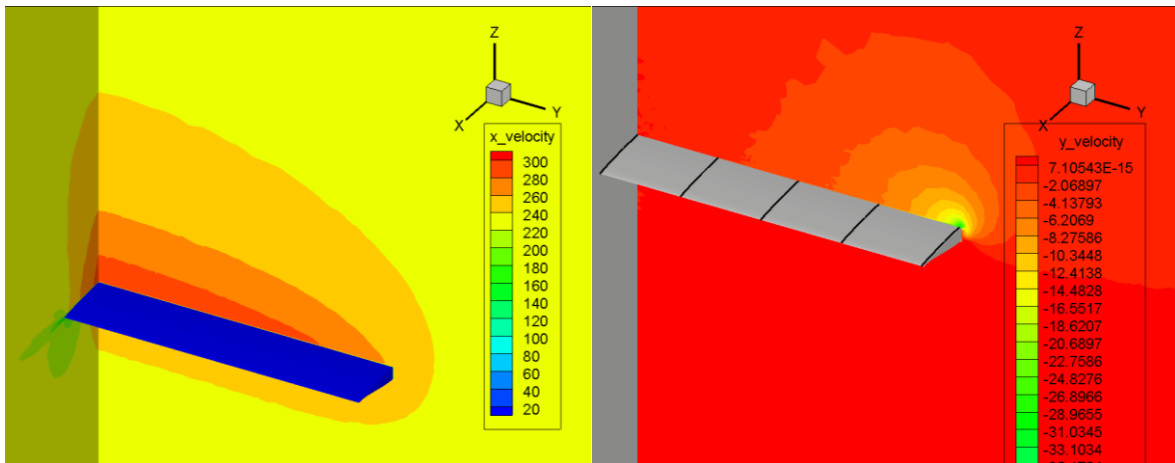


Figure 11: Comparison of MSES result with TAU calculations at several sections for rectangular wing.



(a) Distribution of x-velocity component over the wing at $x/c = 0.5$.

(b) Distribution of y-velocity component over the wing at $x/c = 0.5$.

Figure 12: Velocities in the flow field of the rectangular wing

Next, the swept wing is analyzed. Compared to the rectangular wing, the additional cross-flow component in the direction of the wing tip occurs due to leading edge sweep of the wing. This component weakens the y-component of velocity on the upper side of the wing in the direction from tip to root induced by the vortex. For this reason, the pressure gradient in the leading edge region of the root station (cf. Figure 13) diminishes compared to the one of the rectangular wing, since the velocity in x-direction is lower in this case. In addition, a lower local Mach number due to the leading edge sweep of the wing reduces the overall pressure difference. The pressure distributions at the middle and tip station of the wing are nearly identical to those of the rectangular wing. Here the reduced local Mach number due to wing sweep is compensated by higher velocities in negative y-direction, which results in the same amount of x-velocities as for the rectangular wing at these stations. In case of the tip section, the cross-flow in spanwise direction leads to a higher suction tip in the leading edge region. In addition to the TAU solutions, also the most extreme MSES solutions are presented. As it can be seen, the transformation of flow conditions and geometry with an exponent for the cosine of '1' is the most promising one. Nevertheless, the corrections for considering effects of cross-flow on the wing are not sufficient enough to match the TAU solutions.

Figure 14 illustrates the solution of the flow field around the tapered wing. Since the leading edge sweep is about half of the leading edge sweep of the swept wing, the velocity in x-direction at the leading edge region is higher than for the swept wing, which results in a higher negative pressure on the upper side of the wing for the root and the kink section. For the same reason the cross-flow from root to tip is less pronounced, which results in combination with an increased velocity in x-direction in the same suction peak at the tip section as for the swept wing. In this case of a tapered wing, the tip vortex has a minor strength. In order to that, the flow is less slowed down in the tip and middle section of the wing, which weakens the drawback of the 2D transformations slightly, i.e. not considering these effects. With regard to Eq.5 the 2D Mach number, utilized for MSES calculations, increases with decreasing effective sweep angle. This is the reason, why for the MSES solutions the shock arises at 50 % local chord (cf. solid and dashed lines in Figure 14). The lowest freestream Mach number for MSES calculation is obtained by transforming the freestream conditions with the effective sweep angle of leading edge or trailing edge, respectively.

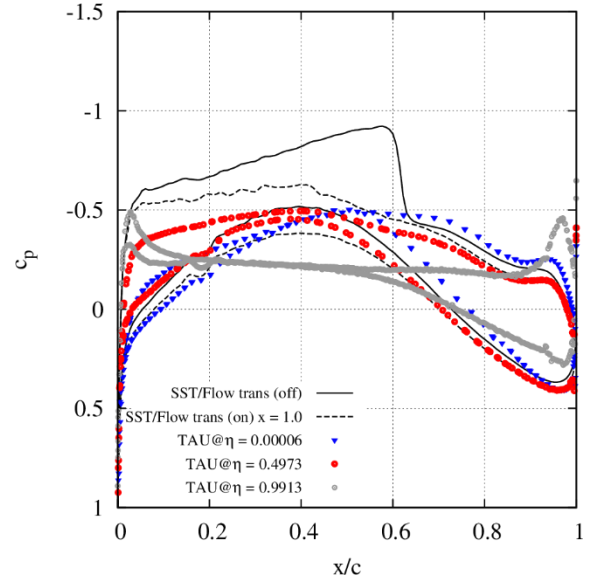


Figure 13: Comparison of MSES result with TAU calculations at several sections for swept wing.

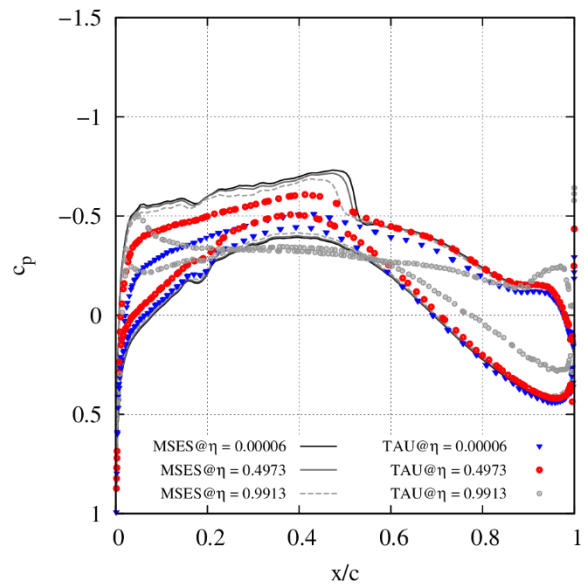


Figure 14: Comparison of MSES results with TAU calculations at several stations for tapered wing.

Applying this, the pressure distributions calculated with MSES match the TAU pressure distribution of the middle section behind the area of recompression. However, applying the proposed method by Boppe to use the sweep angle at the location of recompression area as effective sweep angle would make the pressure distributions calculated with MSES worse compared to those obtained with TAU.

By adding additional sweep to the tapered wing, the pressure distributions get comparable to those of the swept wing (cf. Figure 15). Due to additional taper in comparison to the swept wing, the cross-flow in streamwise direction is developing faster, inducing higher velocities in this region compared to the swept and the tapered wing in the mid- and tip section. Downstream, the strength of the tip vortex is increasing, compensating the lower velocities in x-direction due to higher wing sweep, which results in higher velocities in streamwise direction in each section, as it has already been mentioned in the case of the swept wing. But with a lower local sweep angle at this relative chord position due to the added taper ratio, the cross-flow from the tip to the root is reduced less compared to the swept wing, resulting in higher negative pressure values. Examining the MSES pressure distributions for the tapered-swept wing, a pressure plateau up to the maximum airfoil thickness at 40% local chord can be constituted. The flow is less accelerated, since the transformed airfoil geometry is thinner due to a lower trailing edge angle (cf. Eq.9). In combination with an exponent of '1' for flow correction, this results in pressure deviating from those of TAU calculations. As a solution, an exponent lower than '1' could be chosen, but this would lead to a shock for recompression, since the equivalent 2D freestream Mach number is increased according to Eq.5. Furthermore, this would lead to an increased overall lift, which is not equivalent to the one calculated with TAU.

Finally, Figure 16 shows the pressure distributions for TAU and MSES calculations for the kinked wing. The wing can be treated as an assembly of two swept and tapered wings with a constant leading edge sweep and a different trailing edge sweep regarding spanwise position before and after the kink position. With increased sweep angle of $\varphi_{LE} = 27^\circ$ the cross-flow along the leading edge from the root to the tip section increases. But in this case of a kinked wing, the tip vortex already develops in the leading edge region and reverses the cross-flow in the direction from the tip section to the root section with the same amount as for the tapered-swept wing. This results in a suction peak comparable to the peak for the tapered-swept wing, and due to this also the pressure distribution of the middle section

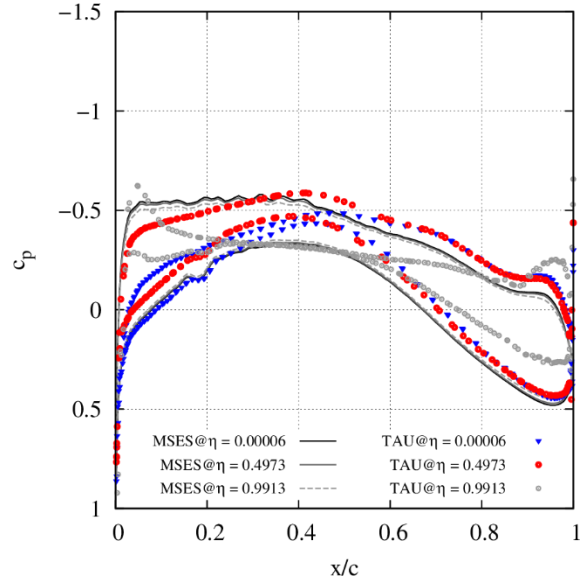


Figure 15: Comparison of MSES results with TAU calculations at several stations for tapered swept wing.

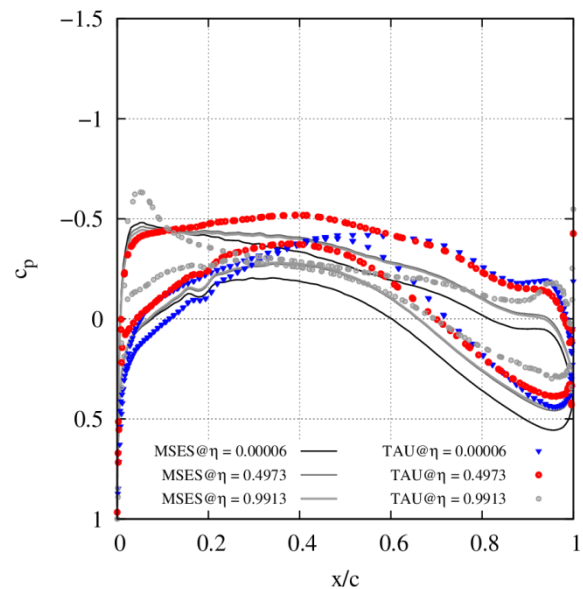


Figure 16: Comparison of MSES results with TAU calculations at several stations for kinked wing.

equals the one of tapered-swept wing. The summation of increased strength of cross-flow in spanwise direction due to applied wing sweep and the one in opposite direction due to the tip vortex, shifts the pressure to slightly less negative values compared to the tapered-swept wing, except for the root section. Due to higher wing sweep in the outboard region of the wing and therefore a reduction of cross-flow from the tip to the root section, the root section is not influenced by the tip vortex anymore. Compared with the tapered-swept wing, the trend of the pressure distributions calculated with MSES becomes worse, if the STT is applied to the kinked wing for MSES calculations with an exponent of '1'. Instead of accelerating the flow behind the nose of the airfoil as it is given by the TAU solution, MSES calculates a deceleration of the flow. This is due to the conical transformation of the airfoil, shrinking the airfoil to a thinner one, which leads in combination with a low 2D freestream Mach number to a deceleration of the flow. By applying SST instead of STT or decreasing the exponent used for considering cross-flow, the pressure distribution calculated with MSES can be adapted.

4 Application of HLFC

After the comparison of different transformation methods with respect to cross-flow with TAU results, in this section the findings will be applied to the kinked wing of a reference aircraft. Therefore, first of all the reference aircraft is introduced. In a second step, the influence of suction in front of the front spar of the kinked wing on the transition line on the wing will be emphasized. Finally, the impact of the different transition lines on block fuel of the overall aircraft will be analyzed.

4.1 Reference aircraft CSR-01

As reference aircraft the CSR-01 will be used within this paper. The CSR-01 is a short range reference aircraft with conventional wing and empennage configuration. The aircraft is designed for a range of 2500 NM and a payload of 17 t. It is powered by two wing-mounted V2527-A5 turbofan engines with a sea-level static thrust of 26500 lbf each. It has been designed with the ILR design platform MICADO. The aircraft design characteristics can be looked up at CeRAS, the Central Reference Aircraft data System, which is a central database hosting reference design data of commercial aircraft. [5], [19] The key aircraft characteristics are listed in Table 3.

Table 3: CSR-01 TLARs and key aircraft characteristics.

Parameter	Symbol	Unit	Value
Design range	R	NM	2500
Design passenger capacity		PAX	150
Design payload	PL	t	17.0
Cruise Mach number	Ma _{cr}	-	0.78
Wing loading	W/S	kg/m ²	629.1
Thrust-to-weight ratio	T/W	-	0.312
Maximum take-off weight	MTOW	t	77.0
Operating weight empty	OWE	t	42.1
Wing area	S _{ref}	m ²	122.4
Wing span	b	m	34.1
Mean aerodynamic chord	MAC	m	4.2
Engine type		-	2x V2527-A5
Sea-level static thrust	SLST	lbf	26500
Block fuel @ design mission	BF	t	14789

The airflow over the wing has been assumed to be fully turbulent. For this paper the original F15-airfoils of the CSR-01 wing were changed to the CRM-airfoil which was analyzed above without changing the key aircraft characteristics.

For the investigation of hybrid laminar flow, a suction system has to be installed on the CSR-01 wing. It will be located in front of the front spar, resulting in different possible suction length due to spanwise position on the wing. The spar positions at the different stations (root, kink, tip) with its relative spanwise position as well as the maximum suction length are given in Table 4.

Table 4: Spar Positions of CSR-01 in % of chord.

Values at Stations	Root	Kink	Tip
Relative spanwise position η	0.0006	0.2870	0.9913
Spar positions [% of chord]	10.7	15.4	27
max. suction length [% of chord]	10	15	25

4.2 Influence of suction to transition line

The pressure distributions of MSES and TAU calculations of the CSR-01 wing were analyzed for laminar flow at each station given in Table 4. Two different type of laminarity will be investigated. First of all, the flow around the airfoils will be examined for Natural Laminar Flow (NLF) and in a second step a suction system is implemented on the wing to attain the maximum possible laminar region. The calculation of laminar area is performed with the program suite STABTOOL from Airbus S.A.S. developed by Geza Schrauf. STABTOOL needs a 3D pressure distribution in streamwise direction as input as well as geometry information of the examined wing (chord, leading/trailing edge sweep) and some information of the flow (Reynolds number, temperature, Mach number). The STABTOOL suite prepares the input for internal usage and performs a boundary layer analysis to calculate laminar velocity and temperature profiles. With these information, a linear stability analysis is performed for each boundary layer profile. Therefore, the e^N - method is implemented in STABTOOL. Finally, an envelope of N-factors is determined by integration of the growth rates of TS-waves and CF-frequencies and combined in a correlation with an envelope of limiting N-factors to determine the transition point. The reader is referred to [24–26] for further information.

The results for a comparison of laminar area obtained for NLF and HLFC are summarized in Table 5.

Table 5: Transition lines in % of chord depending on section and calculation method.

Section	Method	NLF	HLFC
Eta00006	TAU	0.364	0.526
	MSES	0.009	0.231
Eta02870	TAU	0.269	0.645
	MSES	0.147	0.510
Eta09913	TAU	0.093	0.681
	MSES	0.343	0.510

Regarding NLF it is obvious that the differences calculated between TAU and MSES become smaller from root to tip, turning around at tip respectively. This is due to the fact that MSES overestimates the influence of cross-flow at root and underestimates it at the tip. This fact can be underlined with Figure 17. In the upper side of the figure you can see the amplification of cross-flow waves at the tip section for MSES calculation on the left hand side and TAU calculation on the right hand side. Due to the vortex at the wing tip the cross-flow waves for TAU are amplified earlier and also higher than in the case calculated with MSES in which no vortex can be considered. In addition, at the wing tip also the TS-waves develop very fast which results in a small laminar area for TAU in comparison to MSES.

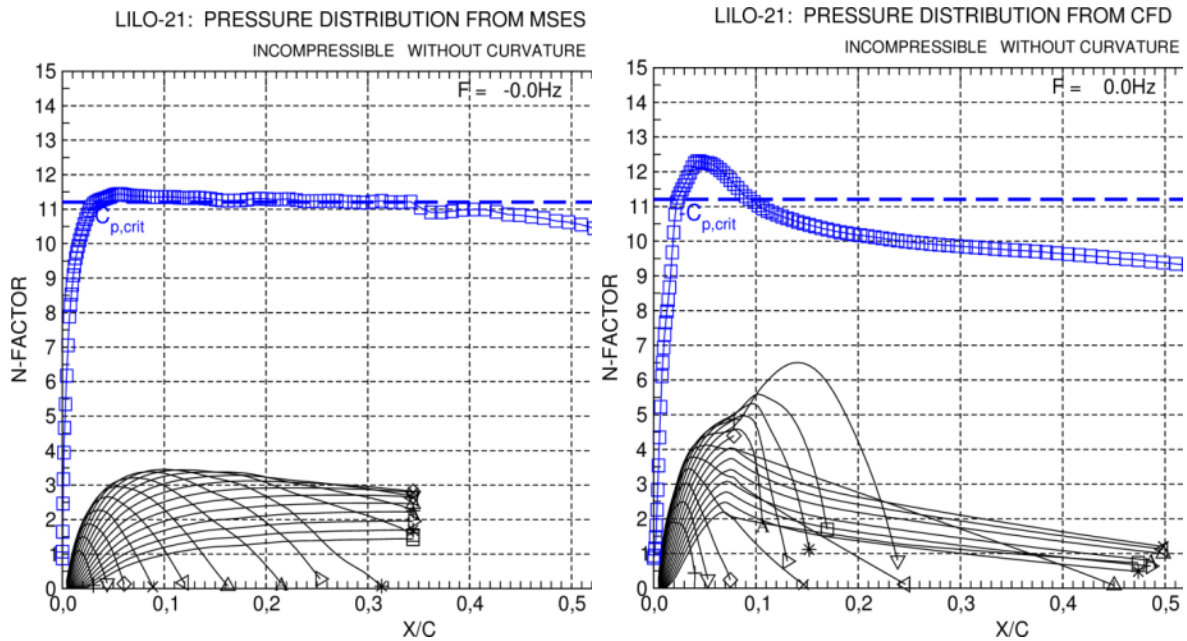


Figure 17: Comparison of CF waves for MSES calculation (left) and TAU calculation (right) at station $\eta=0.9913$

To suppress the CF- and TS-waves for each section and each case a suction distribution has been applied to the flow considering the maximum suction length. The suction was divided into two intervals. The first one starts at the leading edge at a certain strength which is as low as possible to suppress CFI and decreases linear to half of its value over a certain length with the aim to attain the maximum laminar region before laminar separation occurs. The method of suction is derived from several studies [27]. As an example, the suction for the tip segment is given in Figure 18 to suppress CF- and TS-waves for the TAU case. Here the suction starts at the leading edge with strength of

$$C_{Q_s} = \frac{w}{v_\infty} = -0.0008$$

of eight ten-thousandth of freestream velocity normal to the wall of the airfoil. This velocity decreases to half up to 14% of chord where it stagnates up to the end of suction region at 25% of chord. All other suction distributions have been established correspondingly and

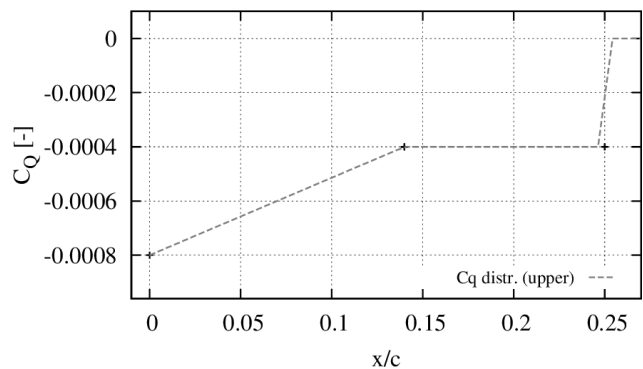


Figure 18: Suction distribution for TAU case at the tip segment

are listed in Table 6. Consistent with the results presented above, the suction at the tip in the case of MSES calculation has to be remarkably lower due to less CF amplification.

Table 6: Suction distributions for each section and case.

Section	Method	Strength at LE [-]	Point of stagnation [% chord]
Eta00006	TAU	-0.0008	0.08
	MSES	-0.00095	0.08
Eta02870	TAU	-0.0008	0.08
	MSES	-0.00095	0.08
Eta09913	TAU	-0.0008	0.14
	MSES	-0.00045	0.08

4.3 Comparison of MSES solution to TAU solution regarding block fuel

The transition lines calculated in section 4.2 have been translated into a laminar area proportional to the reference area of the wing. Therefore the development of laminar region has been assumed linear between the sections which results in laminar areas of the wings presented in Table 7. The percentage of reference area is given in brackets.

Table 7: Laminar area (in % of reference area) depending on calculation method.

Method	NLF	HLFC
TAU	26.078 m ² (0.213)	61 m ² (0.498)
MSES	13.978 m ² (0.114)	42.928 m ² (0.351)

Accounting for these laminar areas the reference aircraft CSR-01 has been redesigned. As for the design, also the redesign of the CSR-01 is conducted with the “Multidisciplinary integrated conceptual aircraft design and optimization environment” (MICADO), developed by the Institute of Aerospace Systems (ILR) of RWTH Aachen University. A detailed description is given in [18]. The integrated sizing approach allows to capture the impact of particular design changes or the integration of innovative systems and technologies, as HLFC, on overall aircraft level, including mass snowball effects and resizing of main aircraft components. MICADO has already been used for several applications in aircraft design and operational studies as well as systems and technology integration and assessment (see e.g. [2, 10, 13–15]).

The savings in block fuel on the same reference mission (same range, flight levels and climb steps as CSR-01) are listed in Table 8.

Table 8: Block fuel decrease due to laminarity w/o HLFC system drawbacks.

Case	Block fuel [kg]	Change to reference [%]
Reference Case	14789	-
TAU (NLF)	14120	- 4.52
MSES (NLF)	14396	- 2.66
TAU (HLFC)	13355	- 9.70
MSES (HLFC)	13740	- 7.09

In cases with natural laminar flow, an overall block fuel saving of 2.66% with MSES is observed and 4.52% with TAU. With an increased laminar area due to HLFC, the saving increase to 7.09% for MSES and 9.7% for TAU, respectively. In these calculations a possible drawback due to the installed HLFC system is not considered yet. If the additional mass of a HLFC system with the additional power off-take of the engines is taken into account and the aircraft is redesigned again, this results in overall block fuel savings which are shown in Table 9: Block fuel decrease due to laminarity with HLFC system drawbacks.

Table 9: Block fuel decrease due to laminarity with HLFC system drawbacks.

Case	Additional System Mass [kg]	Additional Power Offtake [kW]	Blockfuel [kg]	Change to reference [%]
Reference Case	-	-	14789	-
TAU (HLFC)	152.35	38.49	13914	- 5.92
MSES (HLFC)	150.29	34.4	14314	- 3.21

To obtain the maximum laminar area, the HLFC system for the TAU case is only slightly heavier and needs more power offtakes. This reduces the net benefit of block fuel saving to 5.92% and 3.21%, respectively. It can be seen, that the aerodynamic benefit predominates the drawback of the additional HLFC system more for the TAU case than for the MSES case, since the difference in block fuel saving between with and without considering HLFC system drawbacks is less for the TAU case.

5 Conclusion

In this paper the results of investigating the accuracy of 2D methods for estimating laminar flow regions on 3D wing objects were presented. Different transformation methods were utilized to relate 3D and 2D flow and geometry characteristics. For a set of reference wings, the pressure distribution of several wing sections were calculated for all transformation methods and compared to each other. The accuracy of the 2D flow solver MSES in combination with the transformation methods was assessed by comparing the MSES pressure distributions to the TAU solutions of the reference wings. A variation of the exponent in the transformation equations to consider cross-flow as well as the effective sweep angle has demonstrated a) how the approaches differ from each other. The different transformation methods can be used to adapt the thickness of the investigated airfoil as well as the freestream conditions to influence the recompression area in its position and strength as well as the suction peak at the leading edge in a certain amount. Nevertheless, for the analyzed cases the results show that b) the simple estimations and simplifications can be used most likely for flow analysis without any presence of cross-flow. The pressure distributions calculated with MSES showed high deviations from those obtained with TAU solutions, especially for the root and tip region of the wings. In the mid-section of the reference wings the MSES pressure distributions are reasonably comparable with the TAU solution and for the last third of the wing in streamwise direction they exactly match. In the first two thirds of wing sections, the streamwise velocity was overestimated by MSES. These effects could be retrieved in the calculations for the laminar area on the kinked wing and show c) where the limits of these transformation methods are and how far they are from reality. In the case of the kinked wing, the laminar area achieved with TAU solutions as input exceeded the one with MSES solutions as input. Thus, the fuel savings has been estimated 50% less for MSES input. The overall benefit of HLFC technology on overall aircraft level has been shown with fuel savings of about 6% for the TAU solution as input. The results show, that the cross-flow with its effects cannot be fully captured by transformation methods, which relates 2D and 3D flow conditions. By today, the simple taper theory is most likely to be suitable for application in

conceptual aircraft design, relating 2D and 3D flow conditions in areas around the middle section of a conventional airliner wing. But there is no possibility to derive a general approach, which is suitable for all cases. Nevertheless, further investigations are needed in terms of varying flow conditions and airfoils, to be able to derive rules for a potentially better transformation method.

Acknowledgment

The authors thank Geza Schrauf for kindly providing his transition prediction programs. Likewise, we would like to thank Mark Drela for providing the MSES code. Further thanks go to Anna Uhl and all other involved colleagues at ILR.

References

- [1] Anderson, J. D. 2005. *Introduction to flight*. McGraw-Hill, Boston.
- [2] Anton, E., Lammering, T., and Henke, R. 2010. Fast Estimation of Top-Level Requirement Impact on Conceptual Aircraft Designs. In *10th AIAA Aviation Technology, Integration, and Operations (ATIO) Conference*. AIAA.
- [3] Boppe, C. W. 1992. Aircraft drag analysis methods. In *Special Course on Engineering Methods in Aerodynamic Analysis and Design of Aircraft*, Advisory Group for Aerospace Research & Development (AGARD), Ed. AGARD-R-783. NATO, 7.1–8.
- [4] Busemann, A. 1935. Aerodynamischer Auftrieb bei Überschallgeschwindigkeit. In *5. Volta-Kongress*.
- [5] CeRAS. 2014. *Central Reference Aircraft Data System*. <http://ceras.ilr.rwth-aachen.de/>.
- [6] Drela, M. 1985. *Two-Dimensional Transonic Aerodynamic Design and Analysis Using the Euler Equations*. PhD thesis, Massachusetts Institute of Technology (MIT).
- [7] Drela, M. 1994. *MSES Multi-Element Airfoil Design/Analysis Software - Summary*. Massachusetts Institute of Technology (MIT).
- [8] Drela, M. 2007. *A User's Guide to MSES 3.05*. Massachusetts Institute of Technology (MIT).
- [9] European Commission. 2011. *Flightpath 2050 - Europe's Vision for Aviation. Maintaining Global Leadership & Serving Society's Needs Report of the High Level Group on Aviation Research*. Office for Official Publications of the European Communities; EUR-OP, Luxembourg.
- [10] Franz, K., Lammering, T., Risse, K., Anton, E., and Hoernschemeyer, R. 2012. Economics of Laminar Aircraft Considering Off-Design Performance. In *8th AIAA Multidisciplinary Design Optimization Specialist Conference (MDO)*. AIAA.
- [11] Joslin, R. D. 1998. Aircraft Laminar Flow Control. *Annu. Rev. Fluid Mech.* 30, 1, 1–29.
- [12] Küchemann, D. and Weber, J. *The Subsonic Flow Past Swept Wings at Zero Lift Without and With Body*.
- [13] Lammering, T., Anton, E., and Henke, R. 2010. Technology Assessment on Aircraft-Level: Modeling of Innovative Aircraft Systems in Conceptual Aircraft Design. In *10th AIAA Aviation Technology, Integration, and Operations (ATIO) Conference*. AIAA.
- [14] Lammering, T., Anton, E., Risse, K., Franz, K., and Hoernschemeyer, R. 2011. Influence of Off-Design Performance on the Design of Aircraft with Laminar Flow Technology. In *11th AIAA Aviation Technology, Integration, and Operations (ATIO) Conference*. AIAA.
- [15] Lammering, T., Risse, K., Franz, K., Peter, F., and Stumpf, E. 2012. Assessment of Innovative Leading Edge Devices Considering Uncertainties in Conceptual Design. In

- 12th AIAA Aviation Technology, Integration, and Operations (ATIO) Conference.*
AIAA.
- [16] Lock, R. C. 1964. *An Equivalence Law Relating Three- and Two-Dimensional Pressure Distributions* Aeronautical Research Council R&M No. 3346. Her Majesty's Stationery Office, London.
- [17] Poll, D. I. A. 1979. Transition in the infinite swept attachment line boundary layer. *Aeronaut Q* 30, 607–629.
- [18] Risse, K., Anton, E., Lammering, T., Franz, K., and Hoernschemeyer, R. 2012. An Integrated Environment for Preliminary Aircraft Design and Optimization. In *8th AIAA Multidisciplinary Design Optimization Specialist Conference (MDO)*. AIAA.
- [19] Risse, K., Schäfer, K., Schültke, F., and Stumpf, E. 2016. Central Reference Aircraft data System (CeRAS) for research community. *CEAS Aeronaut J* 7, 1, 121–133.
- [20] Rossow, C.-C. 2010. Aerodynamics - A Discipline swept away?, 114, 599–609.
- [21] Saric, W. S. and Yeates, L. G. 1985. Experiments on the Stability of Crossflow Vortices in Swept-Wing Flows. In *23rd AIAA Aerospace Sciences Meeting (ASM)*. AIAA, 1–13. DOI=10.2514/6.1985-493.
- [22] Schlichting, H. and Gersten, K. 2006. *Grenzschicht-Theorie* 10. Springer, Berlin Heidelberg.
- [23] Schlichting, H. and Truckenbrodt, E. 1969. *Aerodynamik des Flugzeuges* 1. Springer, Berlin.
- [24] Schrauf, G. 2000. Evaluation of the A320 hybrid laminar fin experiment. In *European Congress on Computational Methods in Applied Sciences and Engineering*. ECCOMAS.
- [25] Schrauf, G. and Horstmann, K.-H. 2000. Linear Stability Theory Applied to Natural and Hybrid Laminar Flow Experiments. In *Aerodynamic Drag Reduction Technologies. Proceedings of the CEAS/DragNet European Drag Reduction Conference*. Springer, 157–163.
- [26] Schrauf, G., Perraud, J., Vitiello, D., Lam, F., Stock, H.-W., and Abbas, A. 1996. Transition Prediction with Linear Stability Theory - Lessons Learned from the ELFIN F100 Flight Demonstrator. In *2nd European Forum on Laminar Flow Technology*. CEAS.
- [27] Schültke, F. 2014. *Fast and Robust Method for Prediction of Laminar Airfoil Drag Polars*.
- [28] Schwamborn, D. 1981. *Laminare Grenzschichten in der Nähe der Anlegelinie an Flügeln und flügelähnlichen Körpern mit Anstellung* 81-31. DFVLR.
- [29] Staufenbiel, R. 1992. *Luftfahrzeugbau I + II*. Lehrstuhl und Institut für Luft- und Raumfahrt, RWTH Aachen.
- [30] Streit, T., Wichmann, G., von Knoblauch zu Hatzbach, Fedime, and Campbell, R. L. 2011. Implications of Conical Flow for Laminar Wing Design and Analysis. In *29th AIAA Applied Aerodynamics Conference*. AIAA.
- [31] Torenbeek, E. 1982. *Synthesis of Subsonic Airplane Design*. Delft University Press, Delft.
- [32] van Der Velden, A. J. and Kroo, I. M. 1990. A Numerical Method of Relating Two- and Three-Dimensional Pressure Distributions on Transonic Wings. In *AIAA/AHS/ASEE Aircraft Design, Systems and Operations Conference*. AIAA.
- [33] Vassberg, J. C., Haan, M. A. de, Rivers, S. M., and Wahls, R. A. 2008. *Development of a Common Research Model for Applied CFD Validation Studies*.